

# Information fusion and machine learning for sensitivity analysis using physics knowledge and experimental data

Berkcan Kapusuzoglu, Sankaran Mahadevan\*

*Department of Civil and Environmental Engineering, Vanderbilt University, TN 37235*

---

## Abstract

When computational models (either physics-based or data-driven) are used for the sensitivity analysis of engineering systems, the sensitivity estimate is affected by the accuracy and uncertainty of the model. If the physics-based computational model is expensive, an inexpensive surrogate model is built and used to compute the Sobol' indices in variance-based global sensitivity analysis (GSA), and the surrogate model introduces further approximation in the sensitivity estimate. This paper considers GSA for situations where both a physics-based model and a small number of experimental observations are available, and investigates strategies to effectively combine the two sources of information in order to maximize the accuracy and minimize the uncertainty of the sensitivity estimate. Physics-informed and hybrid machine learning strategies are proposed to achieve these objectives. Two machine learning (ML) techniques are considered, namely, deep neural networks (DNN) and Gaussian process (GP) modeling, and two strategies for incorporating physics knowledge within these ML techniques are investigated, namely: (i) incorporating loss functions in the ML models to enforce physics constraints, and (ii) pre-training and updating the ML model using simulation data and experimental data respectively. Four different models are built for each type (DNN and GP), and the uncertainties in these models are also included in the Sobol' indices computation. The DNN-based models, since they have many degrees of freedom in terms of model parameters, are found to result in smaller bounds on the sensitivity estimates when compared to the GP-based models. The

---

\*Corresponding author

Phone: 1-615-322-3040. Fax: 1-615-322-3365. Postal address: Vanderbilt University, VU Station B 356077, Nashville, TN 37235-6077, United States.

*E-mail address:* sankaran.mahadevan@vanderbilt.edu (S. Mahadevan).

proposed methods are illustrated for an additive manufacturing example.

*Keywords:* Global sensitivity analysis, Sobol’ index, Deep learning, Physics-informed machine learning, Additive manufacturing, Fused filament fabrication

---

## 1. Introduction

Computational models are often used to predict the response of an engineering system for a variety of input realizations, since conducting experiments to directly measure the true response for many input realizations is often not affordable. However, the computational model is usually an incomplete representation of the complex physical system, thus the system response prediction is affected by model uncertainty. The various sources of uncertainty are classified as (a) epistemic uncertainty due to lack of knowledge (arising from either data or model inadequacies), and (b) aleatory uncertainty due to the inherent variability in the system properties or the external inputs. Global sensitivity analysis (GSA) [1] aims to provide a quantitative assessment of the relative contribution of each uncertainty source to the uncertainty in the model response [2–4].

Much of the GSA literature has focused on variability in the inputs and their effects on output variability; the extension of GSA to include epistemic uncertainty sources (data, model) is recent and sparse [5, 6]. Model outputs can have uncertainty even for a fixed input when there exists model uncertainty. When the model is computationally expensive, it is often replaced with a surrogate model to facilitate the estimation of Sobol’ indices, since such computation requires many input-output samples from the model; the surrogate model introduces additional uncertainty. Several types of surrogate models are used in the literature, e.g., polynomial chaos expansion (PCE), Gaussian process (GP) regression, neural networks, etc., to train a parametric relationship between the inputs and the outputs. The quality and quantity of the training data affect the accuracy of these surrogate models, which directly affects the uncertainty in the model output [7–9]. Thus, it is important to also include the contribution of surrogate model uncertainty to the output uncertainty in GSA. In Le Gratiet et al [7] for example, the Gaussian process surrogate model uncertainty is included in the Sobol’ index estimates with a

25 Monte Carlo procedure using multiple realizations of the GP model prediction, which helps to  
26 construct prediction intervals for the Sobol' index estimates.

27 In high dimensional problems, even the use of a surrogate model for GSA, which repeatedly  
28 executes the code by suppressing some variables and running through the range of other vari-  
29 ables, may be computationally demanding since the number of executions of the code increases  
30 rapidly with the number of inputs [7, 10–12].

31 Expanding GSA to consider both aleatory and epistemic uncertainty sources is beneficial in  
32 supporting resource allocation decisions. If the contribution of epistemic uncertainty is found  
33 to be significant, then it may be valuable to collect more data or refine the physics model to  
34 reduce the epistemic uncertainty and thus its contribution to the output uncertainty. Several  
35 GSA studies have developed auxiliary variable-based approaches to include both aleatory and  
36 epistemic uncertainty sources at a single level instead of using nested simulations, thus achieving  
37 both computational efficiency and direct ranking of the different sources of uncertainty. The  
38 auxiliary variable is used to transform one-to-many mapping of input to output to one-to-one  
39 mapping, thus facilitating the computation of Sobol' indices for both aleatory and epistemic  
40 sources [5]. This idea is expanded in [6] to include several epistemic sources, such as input  
41 statistical uncertainty, surrogate model error, physics model discrepancy, and numerical solution  
42 error, and to systems with time series inputs and outputs.

43 Three scenarios of model and data availability can be considered for GSA: (1) use of a  
44 physics-based computational model alone, (2) use of available input-output data alone, either  
45 from experiments or previous simulations, or (3) use of both physics model and available input-  
46 output data. A straightforward model-based approach to estimate Sobol' indices is to use  
47 a double-loop Monte Carlo simulation (MCS) [13]. In order to reduce the cost associated  
48 with the double-loop MCS, analytical, spectral and efficient sampling-based methods have been  
49 developed. The methodology developed by Sudret [14] approximates the original physics model  
50 by a PCE and estimates the Sobol' indices by post-processing the PCE coefficients. Chen  
51 et al. [15] proposed analytical formulas to compute Sobol' indices using a GP surrogate model  
52 with input variables following normal or uniform distributions. The improved FAST method [16]

53 combines the classical FAST method [2] with random balanced design [17] for generating samples  
54 to evaluate Sobol' indices.

55 In some problems, input-output data may be already available instead of having to sim-  
56 ulate a physics model expressly for the purpose of GSA. Such data may be available from  
57 experiments, from or real-world observations, or Markov Chain Monte Carlo (MCMC) sampling  
58 during Bayesian model calibration, or MC sampling during reliability analysis, etc. In such  
59 cases, data-driven methods have been proposed to directly compute the Sobol' indices based on  
60 available input-output samples instead of simulation runs of the physics model [10, 18]. A GSA  
61 method based on ANOVA using factorial design of experiments is developed by Ginot et al. [19].  
62 The proposed method results in same values as the Sobol' index since the variance decomposi-  
63 tion used in the Sobol' index estimations is same as the one used in the classical ANOVA [20].  
64 The computational cost of most sample-based methods is proportional to the number of model  
65 inputs. Li and Mahadevan [21] proposed a modularized method, which has a computational  
66 cost that is not proportional to the model input dimension, to estimate the first-order Sobol'  
67 indices based on stratification of available input-output samples. DeCarlo et al. [18] proposed  
68 an importance sampling approach by introducing weights to different data points to estimate  
69 Sobol' indices from available data using Sobol' sequences to reduce the number of simulations;  
70 this method computes both first-order and higher order indices, and is able to include corre-  
71 lated inputs. Approximations to the joint probability distribution of inputs and outputs such  
72 as multivariate Gaussian, Gaussian copula, and Gaussian mixture have recently been found to  
73 give rapid estimation of Sobol' indices [10].

74 The third scenario is of interest in this paper, where both a physics-based model and exper-  
75 imental or real-world data are available. One option, if adequate data is available, is to simply  
76 build a regression or machine learning (ML) model based on the observation data, and use this  
77 model to perform GSA. Multiple recent studies have pursued data-driven machine learning (ML)  
78 models in situations where abundant experimental data or real-world observations are available  
79 due to advances in modern sensing techniques. Generally, the construction of data-driven ML  
80 models does not require in-depth knowledge of the complex physics inherent in the physical

81 process. ML models can learn complex systems using available observations, but the accuracy  
82 of these models depends on the quality and quantity of the data. If the available data is limited,  
83 then the complexity of the process cannot be captured. Further, since purely data-driven ML  
84 models do not explicitly consider physical laws, they can produce physically inconsistent results.  
85 In such cases, incorporating physics knowledge within ML models may improve the accuracy  
86 and efficiency of GSA computations. The combined use of physics-based and ML models has  
87 been shown to achieve more accurate and physically consistent predictions by leveraging the  
88 advantages of each method [22–24].

89 In this work, we incorporate physics knowledge into the ML models to better capture the  
90 physics of the process by leveraging physical laws while improving the generalization perfor-  
91 mance of data-driven models. Two types of strategies are considered for incorporating physics  
92 knowledge within ML models: (1) incorporating loss functions in the ML model training to  
93 enforce physics constraints, and (2) pre-training the ML model with data generated by the  
94 physics model and then updating it with experimental data. Note that the first strategy does  
95 not use the physics model but only constraints for the output to obey physical requirements;  
96 whereas, the second strategy explicitly uses the physics computational model. Two types of  
97 ML models are considered in this paper, namely, GP and DNN. Four different physics-informed  
98 machine learning (PIML) models are developed for each type (i.e., GP or DNN) to predict the  
99 output quantity of interest (QoI), through combinations of the two strategies. The resulting  
100 GSA procedure includes the effect of uncertainty in the ML or PIML model.

101 In summary, the contributions of this paper are as follows:

- 102 • Physics knowledge and experimental observations are fused in order to maximize the ac-  
103 curacy and minimize the uncertainty of sensitivity estimates.
- 104 • Two PIML strategies and their combinations are investigated for sensitivity analysis using  
105 both physics knowledge and experimental data.
- 106 • Four different models are built for each of GP and DNN, and the uncertainties in these  
107 models are included in the Sobol’ indices computation.

- The accuracy, uncertainty and computational effort of different options for ML and PIML models are evaluated and compared.

The outline of the rest of this paper is as follows. Section 2 provides background information on related methods. Section 3 presents the proposed methodology. The proposed methodology is illustrated for a numerical example in Section 4. Concluding remarks are provided in Section 5.

## 2. Background

This section introduces each of the basic techniques used in developing the proposed methodology, namely variance-based GSA, Gaussian process surrogate modeling, and deep neural networks (DNN). These techniques are well established with extensive literature, therefore only a brief introduction is given here.

### 2.1. Variance-based GSA

Consider a deterministic real integrable one-to-one system response function  $Y = f(\mathbf{X})$ , where  $f(\cdot)$  is the computational model,  $\mathbf{X} = \{X_1, \dots, X_k\}$  are mutually independent model inputs, and  $Y$  is the model output. As shown in [13], the variance of  $Y$  can be decomposed as

$$V(Y) = \sum_i^k V_i + \sum_{i_1}^k \sum_{i_2=i_1+1}^k V_{i_1 i_2} + \sum_{i_1}^k \sum_{i_2=i_1+1}^k \sum_{i_3=i_2+1}^k V_{i_1 i_2 i_3} + \dots + V_{12\dots k} \quad (1)$$

where  $V_i$  is the variance of  $Y$  due to  $X_i$  alone, and  $V_{i_1\dots i_p}$  ( $p \geq 2$ ) indicates the variance of  $Y$  due to  $\{X_{i_1}, \dots, X_{i_p}\}$ .

The Sobol' indices are defined by dividing both sides of Eq. (1) with  $V(Y)$

$$1 = \sum_i^k S_i + \sum_{i_1}^k \sum_{i_2=i_1+1}^k S_{i_1 i_2} + \sum_{i_1}^k \sum_{i_2=i_1+1}^k \sum_{i_3=i_2+1}^k S_{i_1 i_2 i_3} + \dots + S_{12\dots k} \quad (2)$$

where  $S_i$  is the first-order or main effects index that assesses the contribution of  $X_i$  individually to the variance of the output  $Y$  without considering interactions with other inputs. The higher-order indices  $S_{i_1\dots i_p}$  ( $p \geq 2$ ) in Eq. (2) measure the contributions of individual plus interactive effects of  $\{X_{i_1}, \dots, X_{i_p}\}$ .

The first-order index  $S_i$  is defined as follows:

$$S_i = \frac{V_i}{V(Y)} = \frac{V_{X_i}(E_{\mathbf{X}_{-i}}(Y|X_i))}{V(Y)} \quad (3)$$

where  $\mathbf{X}_{-i}$  are all the model inputs other than  $X_i$ .

The overall contribution of  $X_i$  considering an individual input and its interactions with all other inputs is measured by the total effects index  $S_i^T$ :

$$S_i^T = 1 - \frac{V_{-i}}{V(Y)} = \frac{V_{\mathbf{X}_{-i}}(E_{X_i}(Y|\mathbf{X}_{-i}))}{V(Y)}. \quad (4)$$

The computation of  $S_i$  analytically is nontrivial since  $E_{\mathbf{X}_{-i}}(\cdot)$  requires multi-dimensional integrals. A basic sampling-based approach is to use double-loop sampling [13]. Several approaches to reduce the computational cost were mentioned in Section 1. One of these approaches of particular relevance to this paper is to replace the original computational model  $f(\cdot)$  by a surrogate model and use this surrogate model in GSA [25–29]. This approach will be discussed further in Section 3.

## 2.2. Gaussian process surrogate modeling

The GP surrogate model provides a prediction  $f(\mathbf{u})$  at a given input  $\mathbf{u}$  as

$$f(\mathbf{u}) = \mathbf{h}(\mathbf{u})^T \boldsymbol{\beta} + z(\mathbf{u}) \quad (5)$$

where  $\mathbf{h}(\cdot)$  is the trend function,  $\boldsymbol{\beta}$  is the vector of trend coefficients, and  $z(\cdot)$  is a random variable from a zero mean GP with covariance function, which describes the deviation of the model from the trend. The covariance between the outputs of the Gaussian process  $Z(\cdot)$  at points  $\mathbf{a}$  and  $\mathbf{b}$  is defined as:

$$\text{Cov}[Z(\mathbf{a}), Z(\mathbf{b})] = \sigma_Z^2 R(\mathbf{a}, \mathbf{b}) \quad (6)$$

141 where  $\sigma_Z^2$  is the process variance and  $R(\cdot, \cdot)$  is the correlation function. A squared exponential  
 142 correlation function with separate length scale parameters  $l_i$  for each input dimension has often  
 143 been used in the literature:

$$R(\mathbf{a}, \mathbf{b}) = \exp \left[ - \sum_{i=1}^M \frac{(a_i - b_i)^2}{l_i} \right] \quad (7)$$

The hyperparameters of the GP model, i.e.,  $\Theta = \{l, \sigma_Z, \sigma_{obs}\}$ , where  $\sigma_{obs}$  is the observation error, are inferred from the training data. A common method is to maximize the log marginal likelihood function, which is defined as

$$\log p(\mathbf{Y}|\mathbf{X}; \Theta) = -\frac{1}{2}\mathbf{Y}(\mathbf{K}_{TT} + \sigma_{obs}^2\mathbf{I})^{-1}\mathbf{Y} - \frac{1}{2}\log|\mathbf{K}_{TT} + \sigma_{obs}^2\mathbf{I}| + \frac{n}{2}\log 2\pi. \quad (8)$$

144 The outputs of the GP model are the mean prediction  $\mu_G(\cdot)$  and the variance of the prediction  
 145  $\sigma_G^2(\cdot)$ , defined as:

$$\mu_G(\mathbf{u}) = \mathbf{h}(\mathbf{u})^T \boldsymbol{\beta} + \mathbf{r}(\mathbf{u})^T \mathbf{R}^{-1}(\mathbf{g} - \mathbf{F}\boldsymbol{\beta}) \quad (9)$$

$$\sigma_G^2(\mathbf{u}) = \sigma_Z^2 - \mathbf{A} \begin{bmatrix} \mathbf{0} & \mathbf{F}^T \\ \mathbf{F} & \mathbf{R} \end{bmatrix}^{-1} \mathbf{A}^T \quad (10)$$

147 where  $\mathbf{r}(\mathbf{u})$  is a vector containing the covariance between  $\mathbf{u}$  and each of the training points  
 148  $\{x_1, x_2, \dots, x_n\}$ ,  $i \in \{1, \dots, n\}$ ,  $\mathbf{R}$  is an  $n \times n$  matrix containing the correlation between each pair of  
 149 training points,  $\mathbf{R}(x_i, x_j) = \text{Cov}[Z(x_i), Z(x_j)]$ ;  $\mathbf{g}$  is the vector of original physics model outputs  
 150 at each of the training points,  $\mathbf{F}$  is a  $n \times q$  matrix with rows  $\mathbf{h}(\mathbf{u}_i)^T$ , and  $\mathbf{A} = [\mathbf{h}(\mathbf{u})^T \mathbf{r}(\mathbf{u})^T]$ .

### 151 2.3. Deep neural networks

152 In recent years, due to the confluence of advanced sensing and imaging techniques, big  
 153 data processing techniques, enormous computational power and the internet, rapid advances  
 154 are being made in developing sophisticated data-driven machine learning models, particularly  
 155 neural networks. A deep neural network (DNN) is composed of multiple hidden layers and has  
 156 four major components: neuron, activation function, cost function, and optimization. Figure 1



157 shows a neural network consisting of three inputs, two hidden layers, each having four neurons,  
 158 and two output neurons. The values of various input variables of a particular neuron are  
 159 multiplied by their associated weights, then the sum of the products of the neuron weights and  
 160 the inputs are calculated at each neuron. The summed value is passed through an activation  
 161 function that maps the summed value to a fixed range before passing these signals on to the  
 next layer of neurons.

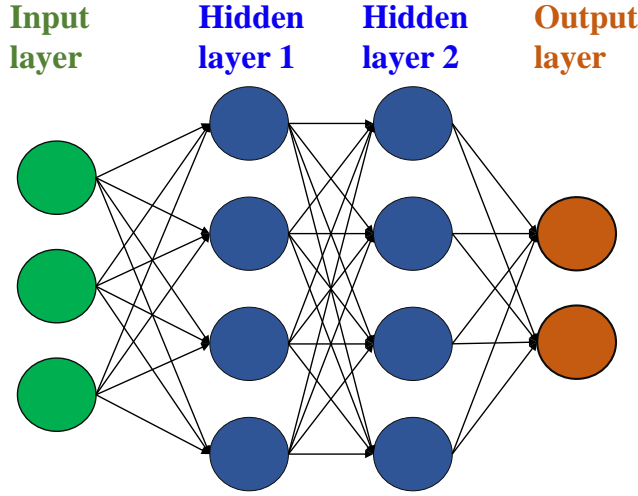


**Fig. 1.** A deep neural network with two hidden layers.

162

163 The predictions of the DNN after a forward propagation,  $\hat{\mathbf{Y}}$ , are compared against the true  
 164 response of the system,  $\mathbf{Y}$ , by defining a loss function (e.g., root mean squared error (RMSE));  
 165  $\mathcal{L}_{\text{RMSE}}(\mathbf{Y}, \hat{\mathbf{Y}}) = \sqrt{\sum_{i=1}^n (y_i - \hat{y}_i)^2 / n}$ , which measures how far off the predictions are from the  
 166 observations for the  $n$  training samples. Backpropagation algorithms are employed to keep track  
 167 of small perturbations to the weights that affect the error in the output and to distribute this  
 168 error back through the network layers by computing gradients for each layer using the chain rule.  
 169 In order to minimize the value of the loss function, necessary adjustments are applied at each  
 170 iteration to the neuron weights in each layer of the network. These procedures are performed  
 171 at each iteration until the loss function converges to a stable value.

### 3. Proposed methodology

The proposed methodology for sensitivity analysis using both physics knowledge and experimental data consists of the following steps:

1. PIML strategies
2. Implementation of PIML in GP
3. Implementation of PIML in DNN
4. Model uncertainty quantification in GP and DNN
5. Sobol' indices computation with model uncertainty

The following subsections describe these steps in detail.

#### 3.1. PIML strategies

PIML models seek to incorporate physics knowledge or constraints within the data-driven ML models. When a mechanistic, physics-based model is also available, complementary strengths of both mechanistic and ML models can be leveraged in a synergistic manner [24]. In the latter case, the aim is to improve the predictions beyond that of physics-based models or ML models alone by coupling physics-based models with ML models. Thus two different strategies to combine physics knowledge and ML models can be considered: (1) incorporate physics constraints in the ML models, and (2) pre-train and update the ML models using physics model input-output and experimental data, respectively.

##### 3.1.1. Strategy 1: Enforcing physics constraints

A direct strategy to enforce physics constraints in ML model predictions is by including the constraints in the loss functions used in training the ML model [22]. Consider a PIML model with inputs  $\mathbf{X}$  and outputs  $\hat{\mathbf{Y}}$  trained using physical laws that are incorporated as constraints into the loss function:

$$\mathcal{L} = \mathcal{L}_{\text{ML}} + \lambda_{\text{phy}} \mathcal{L}_{\text{phy}}(\hat{\mathbf{Y}}), \quad (11)$$

191 where  $\mathcal{L}_{\text{ML}}$  is the log marginal likelihood of the data for a GP model:

$$\mathcal{L}_{\text{GP}} = \log p(\mathbf{Y}|\mathbf{X}; \boldsymbol{\Theta}) \quad (12)$$

192 and regular training loss function for a DNN that evaluates a supervised error, e.g., root mean  
193 squared error (RMSE):

$$\mathcal{L}_{\text{DNN}}(\mathbf{Y}, \hat{\mathbf{Y}}) = \sqrt{\sum_{i=1}^n \frac{(Y_i - \hat{Y}_i)^2}{n}} \quad (13)$$

194 which measures the accuracy of predictions  $\hat{\mathbf{Y}}$  for  $n$  training samples. (Note that for the GP  
195 model, the likelihood is maximized, whereas for the DNN model, the RMSE is minimized).  
196 The additional physics constraint loss function  $\mathcal{L}_{\text{phy}}$  in the second term of Eq. 11 is weighted  
197 by a hyperparameter  $\lambda_{\text{phy}}$ ; the value of  $\lambda_{\text{phy}}$  controls the strength of the physics constraint  
198 enforcement. The inclusion of the second term ensures physically consistent model predictions  
199 and helps to reduce the generalization error, which is a measure of how accurately a model is  
200 able to predict the output QoI for previously unseen data [22].

The physical inconsistencies in the model predictions are evaluated using the physics constraint loss term. The generic forms of these physical relationships can be expressed using the following constraints:

$$\begin{aligned} \mathcal{F}_1(\hat{\mathbf{Y}}, \boldsymbol{\Gamma}) &= 0, \\ \mathcal{F}_2(\hat{\mathbf{Y}}, \boldsymbol{\Gamma}) &\leq 0. \end{aligned} \quad (14)$$

where  $\boldsymbol{\Gamma}$  denotes model parameters. These equations can involve algebraic relationships or partial differentials of  $\hat{\mathbf{Y}}$  and  $\boldsymbol{\Gamma}$ . The physics-based loss functions for these equations can be defined as:

$$\mathcal{L}_{\text{phy}}(\hat{\mathbf{Y}}) = \|\mathcal{F}_1(\hat{\mathbf{Y}}, \boldsymbol{\Gamma})\|^2 + \text{ReLU}(\mathcal{F}_2(\hat{\mathbf{Y}}, \boldsymbol{\Gamma})), \quad (15)$$

201 where  $\text{ReLU}(x) = \max(0, x)$  represents the rectified linear unit function and it is used here to

specify an allowable range of values; it penalizes the optimization when the difference between the predicted and target values are larger than the threshold. It can also be used to penalize derivations from a desired physically consistent relationship among multiple outputs  $\hat{\mathbf{Y}}$  [30].

### 3.1.2. Strategy 2: Pre-training and Updating

The ML model output accuracy and uncertainty are dependent on the quality and quantity of the available training data. In some systems, the high cost associated with conducting experiments makes it infeasible to have adequate amount of training data to build purely data-driven models. Thus, it is important to effectively combine the physics-based model and available experimental data in order to maximize the accuracy and minimize the uncertainty of the sensitivity estimate. When the experiments are expensive, they can only be conducted for a few values of the inputs, whereas it might be possible to run the physics-based model for multiple combinations of input values. In that case, the simulation data can be used to pre-train an ML model, which is used as the initial model to be updated with experimental observations. Further, training of ML models requires the choice of initial values of the model parameters. The transfer of physical knowledge using a pre-trained ML model can prevent poor initialization due to lack of knowledge regarding the initial choice of ML model parameters prior to training.

Since the pre-training based on the mechanistic model can use a large amount of training data (with multiple input parameter combinations) over a wide range of values, the pre-training may also help the eventual ML model to have wider generalization beyond experimental data. In the numerical example in Section 4, the pre-training strategy exercises the physics model over 1310 input combinations, whereas only 39 experiments are available. However, if the physics model is computationally expensive, then the advantage of the pre-training strategy in using a larger input data set (from physics model runs) compared to the experiments becomes limited.

The two proposed strategies to predict the QoI are shown in Fig. 2. Figure 2(a) shows the first method, where the physical knowledge is included through constraints within the loss function of an ML trained with experimental data. Figure 2(b) shows the second method, where an ML model is first trained with data generated using the physics-based model and then

updated using experimental data. The proposed PIML strategies can be applied to any physical system by leveraging the related physical constraints or physics-based models.

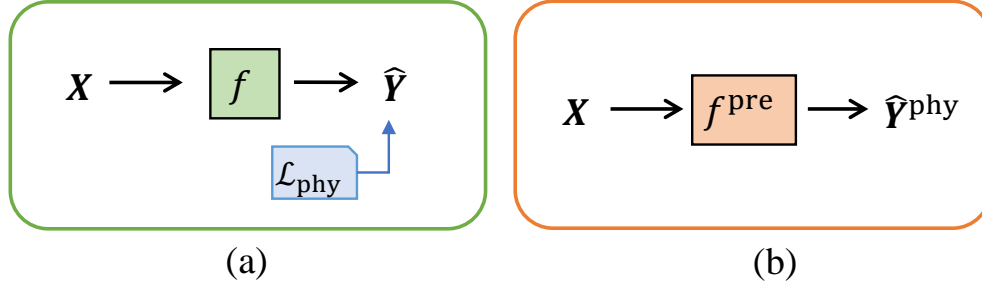


**Fig. 2.** PIML strategies: (a) incorporating physics-based loss functions in the ML models to enforce physics constraints, (b) pre-training an ML model with physics model input-output and updating it with experimental data.

230

### 231 3.2. Implementation of PIML strategies in GP and DNN

232 Based on the proposed two strategies to incorporate physics knowledge into the ML model,  
233 four separate ML models can be constructed for each type of surrogate model (GP and DNN):

- |   |  |
|---|--|
| 234 1. GP   | 238 5. DNN   |
| 235 2. $\text{GP}^{\mathcal{L}_{\text{phy}}}$             | 239 6. $\text{DNN}^{\mathcal{L}_{\text{phy}}}$             |
| 236 3. $\text{GP}^{\text{upd}}$                           | 240 7. $\text{DNN}^{\text{upd}}$                           |
| 237 4. $\text{GP}^{\text{upd}, \mathcal{L}_{\text{phy}}}$ | 241 8. $\text{DNN}^{\text{upd}, \mathcal{L}_{\text{phy}}}$ |

242 The implementations of PIML strategies 1, 2, and their combination are different for the GP  
243 models vs. the DNN models. The following subsections describe how the PIML strategies can  
244 be implemented for each of the above models.

#### 245 3.2.1. Implementation of PIML in GP

246 In the first model, GP, only experimental observations are used for training. The hyper-  
247 parameters are optimized during training by maximizing the log marginal likelihood function  
248 shown in Eq. 8. The difference between the true response of the system  $\mathbf{Y}_{\text{true}}$  and observations  
249  $\mathbf{Y}_{\text{obs}}$  is attributed to observation error  $\epsilon_{\text{obs}}$ , which is often treated as a zero-mean Gaussian  
250 random variable with variance  $\sigma_{\text{obs}}^2$ .

Model 2, denoted as  $\text{GP}^{\mathcal{L}_{\text{phy}}}$  above, incorporates the first strategy by enforcing physics constraints during the optimization of GP model hyperparameters. More specifically, the physics constraints are included in the maximization of the log marginal likelihood function (Eq. (8)) while inferring the hyperparameters of the GP model; thus constrained optimization is implemented. Specifically, the training of the model 2 is achieved by maximizing the function given in Eq. 16:

$$\mathcal{L}_{\text{GP}} = \log p(\mathbf{Y}|\mathbf{X}; \boldsymbol{\Theta}) - \lambda_{\text{phy}} \mathcal{L}_{\text{phy}}(\hat{\mathbf{Y}}), \quad (16)$$

251 where  $\hat{\mathbf{Y}}$  is the GP model predictions.

252 Model 3,  $\text{GP}^{\text{upd}}$ , where the second PIML strategy is pursued, pre-trains a GP surrogate model  
 253 with data generated from the physics model, then improves the surrogate using experimental  
 254 data. Consider a physics model  $G(\cdot)$  that maps input variables  $\mathbf{X}$  and model parameters  $\boldsymbol{\theta}_m$  to  
 255 the numerical model output  $\mathbf{Y}_m$ :

$$\mathbf{Y}_m = G(\mathbf{X}; \boldsymbol{\theta}_m(\mathbf{X})). \quad (17)$$

256 Let  $n_D$  be the number of collected observation data  $\mathbf{Y}_{\text{obs}}$  from experiments with input variable  
 257 settings  $\mathbf{x}^{(1)}, \dots, \mathbf{x}^{(n_D)}$ , where  $\mathbf{x}^{(i)}$  is the input variable setting for the  $i$ th experiment. The physics  
 258 model prediction is inaccurate due to missing physics or due to other approximations. Thus,  
 259 a model discrepancy term  $\boldsymbol{\delta}(\mathbf{X})$  as a function of model inputs is introduced to capture the  
 260 difference between  $\mathbf{Y}_{\text{true}}$  and  $\mathbf{Y}_m$  [31]. The true system response  $\mathbf{Y}_{\text{true}}$  can be described as

$$\mathbf{Y}_{\text{true}}(\mathbf{X}) = \mathbf{Y}_{\text{obs}}(\mathbf{X}) + \epsilon_{\text{obs}}(\mathbf{X}) = \mathbf{Y}_m(\mathbf{X}) + \boldsymbol{\delta}(\mathbf{X}) = G(\mathbf{X}; \boldsymbol{\theta}_m(\mathbf{X})) + \boldsymbol{\delta}(\mathbf{X}). \quad (18)$$

261 When the physics model is computationally expensive, it is replaced by a cheaper surrogate  
 262 model. In Model 3, a GP surrogate model is used to approximate the original physics model.  
 263 The accuracy of the surrogate model prediction depends on the quality and quantity of the  
 264 training data generated by the original physics model. The surrogate model error ( $\epsilon_{\delta}$ ) can be

265 incorporated as follows:

$$\mathbf{Y}_m(\mathbf{X}) = \hat{\mathbf{Y}}_m(\mathbf{X}) + \epsilon_\delta, \quad (19)$$

266 where  $\hat{\mathbf{Y}}_m$  is the surrogate model prediction.

267 A common approach to estimate the discrepancy term is the one formulated by Kennedy and  
268 O’Hagan [31], which is applicable in the context of Bayesian calibration. In that case, physics  
269 model parameters are sought to be calibrated, and a discrepancy term is added in the calibration  
270 equation. The discrepancy term can be expressed in multiple ways, such as constant, Gaussian  
271 random variable with unknown parameters (either input-dependent or not), or Gaussian process  
272 (either stationary or non-stationary) [32]. The hyperparameters of the discrepancy term are then  
273 estimated along with the physics model parameters using Bayesian calibration. However, the  
274 situation considered here is much simpler. There is no calibration of physics model parameters  
275 here; only the discrepancy term is needed. (In other words, the physics model parameters are  
276 already established). In that case, the model discrepancy can be evaluated for different input  
277 values of experimental tests and realizations of observation errors as follows:

$$\delta(\mathbf{X}) = \mathbf{Y}_{\text{obs}}(\mathbf{X}) + \epsilon_{\text{obs}}(\mathbf{X}) - \hat{\mathbf{Y}}_m(\mathbf{X}) - \epsilon_\delta. \quad (20)$$

278 In this work, a simplified approach is pursued by quantifying the overall model error instead  
279 of quantifying the individual error terms  $\epsilon_\delta$  and  $\epsilon_{\text{obs}}$ .

280 Following this, a second GP model can be trained for the discrepancy term in terms of the  
281 inputs. Thus two GP models are trained in Model 3: (i) the first GP model replaces the physics  
282 model to predict the QoI; and (ii) the second GP model is constructed for the discrepancy term  
283  $\hat{\delta}$  (i.e., the difference between the surrogate model prediction and actual system response) using  
284 experimental data.

285 The GP model for the model discrepancy captures the combined contribution of measurement  
286 error, physics and surrogate model errors for a given prediction. Thus, the predictions of the first  
287 GP model (pre-trained) are corrected with the second GP model predictions ( $\hat{\delta}$ ) representing

the model discrepancy term and can be written as

$$\hat{\mathbf{Y}}_{corr}(\mathbf{x}) = \hat{\mathbf{Y}}_m(\mathbf{X}) + \hat{\boldsymbol{\delta}}. \quad (21)$$

Model 4 is a combination of the two strategies, in which both the pre-trained model is corrected with  $\hat{\boldsymbol{\delta}}$  and physics constraints are enforced. First, the first GP model is trained using the physics samples to predict the QoI. Then, using the experimental data the second GP model is constructed by enforcing physics constraints during the optimization of its hyperparameters. This involves prediction using both first and second GP models and checking the output against the physics constraints. However, only the hyperparameters of second GP model are affected by these physics constraints.

### 3.2.2. Implementation of PIML in DNN

In Model 5, denoted simply as DNN, a DNN is trained using only experimental data. In order to train the model, an optimization algorithm is used to find a set of model parameters (weights and biases) that best map inputs to outputs.

Model 6, denoted as  $\text{DNN}^{\mathcal{L}_{\text{phy}}}$ , extends Model 5 by implementing the first PIML strategy, i.e., physical knowledge related to the physical process is enforced through constraints within the loss function of the DNN, as shown in Eq. 11. The physics-based loss functions are evaluated for given physics inputs at every optimization iteration during the training of  $\text{DNN}^{\mathcal{L}_{\text{phy}}}$ ; thus it creates additional challenges by slowing down the optimization process during training. The multipliers of the physics constraint terms ( $\lambda_{\text{phy}}^{\text{DNN}}$ ) affect the training of the network by putting more importance on the physics constraints.

Model 7, denoted as  $\text{DNN}^{\text{upd}}$ , pursues the second PIML strategy, where a DNN model is pre-trained using the coupled multi-physics model input-output and then updated with experimental data. The pre-trained model is first trained with physics model input-output data consisting of input combinations over a range of values. Then, the weights and biases (model parameters) of this pre-trained network are updated using the experimental data. Note that the model parameters in this case are updated using a least squares approach, whereas in the GP approach



(i.e., in Model 3  $\text{GP}^{\text{upd}}$  and Model 4  $\text{GP}^{\text{upd}, \mathcal{L}_{\text{phy}}}$ ), a discrepancy term  $\hat{\delta}$  is constructed using the experimental data and added to the first GP model trained with physics model input-output.

Model 8, denoted as  $\text{DNN}^{\text{upd}, \mathcal{L}_{\text{phy}}}$ , is a combination of the two PIML strategies for DNN, where the optimized model parameters of the pre-trained model based on the physics model input-output are used as the initial values. These model parameters are updated using the experimental data by minimizing the regular training loss function shown in Eq. 13 together with the physics-based loss functions. Similar to model 6, the inclusion of physics constraints makes it more challenging for the optimization to converge to optimal model parameter values.

### 3.3. Model uncertainty quantification in GP and DNN

In general terms what is the fit a model to data, any regression model has uncertainty. In the GP, the uncertainty is reflected by this GP. One way to quantify uncertainty in GP is by generating many samples of GP. at any given  $\mathbf{x}$  the prediction is normal dist.

In the DNN models, the estimates of the model parameters (neuron weights  $\mathbf{w}$ ) have uncertainty, and this uncertainty depends on the available training data. When the network's parameters are represented using distributions (to reflect the epistemic uncertainty) instead of deterministic values, the model is referred to as a Bayesian neural network (BNN) [33–35]. In this Bayesian context, the model parameter uncertainty is first described using a prior distribution  $p(\mathbf{w})$ , and the likelihood function is  $p(\mathbf{Y}|\mathbf{X}, \mathbf{w})$ . (A commonly used prior distribution is Gaussian, i.e.,  $p(\mathbf{w} = \mathcal{N}(0, \mathcal{I}))$ ). Following Bayes' theorem, a posterior distribution over the model parameters given the training data  $\{\mathbf{X}, \mathbf{Y}\} = \{\{\mathbf{x}_1, \dots, \mathbf{x}_N\}, \{\{\mathbf{y}_1, \dots, \mathbf{y}_N\}\}$  is defined by

$$p(\mathbf{w}|\mathbf{X}, \mathbf{Y}) = \frac{p(\mathbf{Y}|\mathbf{X}, \mathbf{w})p(\mathbf{w})}{p(\mathbf{Y}|\mathbf{X})}. \quad (22)$$

In this context, the predictive distribution of the model outputs for a given input  $\mathbf{x}^*$  is given by:

$$p(\mathbf{y}^*|\mathbf{x}^*, \mathbf{X}, \mathbf{Y}) = \int_{\Omega} p(\mathbf{y}^*|\mathbf{x}^*, \mathbf{w})p(\mathbf{w}|\mathbf{X}, \mathbf{Y})d\mathbf{w}. \quad (23)$$

The posterior distribution of model parameters  $p(\mathbf{w}|\mathbf{X}, \mathbf{Y})$  is challenging to evaluate over the

entire parameter space  $\Omega$  due to the high dimensionality of  $\Omega$ , and the highly non-linear behavior in the neural network caused by the non-linear activation functions and their combinations across multiple hidden layers.

Therefore, different approximate inference techniques can be considered to infer the posterior distribution  $p(\mathbf{w}|\mathbf{X}, \mathbf{Y})$  [36–39]. One such approximation is variational inference, which fits a simple and tractable distribution  $q_{\theta}(\mathbf{w})$  to the posterior, parametrized by a variational parameter  $\theta$  [36]. This approximates the intractable problem by optimizing the parameters of  $q_{\theta}(\mathbf{w})$ . The closeness of the variational distribution is often measured by the Kullback-Leibler (KL) divergence between the approximate distribution  $q_{\theta}(\mathbf{w})$  and the true model posterior  $p(\mathbf{w}|\mathbf{X}, \mathbf{Y})$ .

The term *dropout* refers to randomly dropping out neurons (along with their connections) with a given dropout rate during the training phase in a neural network. Dropout is a common regularization approach in neural network training, which prevents over-fitting and reduces generalization error. A Monte Carlo (MC) dropout technique has been developed in recent years [40] which has been shown to be equivalent to performing approximate variational inference. In MC dropout, dropout is not only applied while training a model but also during prediction. Randomly chosen neurons are temporarily removed from the network along with their connections. Next, the gradients of neurons weights are calculated on a sub-neural network for each training data and these gradients are then averaged over the training sets to obtain the weights for the overall network. In contrast to standard neural networks, the MC dropout performs dropout and generates random samples following a binomial distribution (0 or 1) for each neuron in the input and hidden layers during prediction. The neuron that takes the value 0 is dropped out with a given dropout probability  $p_d$ . The outputs of the network are predicted using the collection of generated random samples from the posterior predictive distribution and the uncertainty in the prediction of a new data is quantified with the trained network. Thus the MC dropout strategy provides an efficient way of Bayesian inference to quantify the model prediction uncertainty, and can be applied to a variety of neural networks, such as feedforward neural networks, convolutional neural networks, and recurrent neural networks [41].

The sensitivity estimate results depend on the dropout rate. The main-effect of variables

continuously diminishes as dropout rate increase. The main reason for this is that the model is over-regularized; thus it is underfitting, which means there is still room for improvement on the test data.

### 3.4. Sobol' indices computation with model uncertainty

As discussed earlier, often in physics-based and data-driven models it is necessary to quantify the model uncertainty and its contribution to the Sobol' index estimates. In this section, we present the inclusion of model uncertainty in the Sobol' index estimates.

Every surrogate model has uncertainty in the prediction. In a noise free model, the GP predictions at the training points have zero variance and at other points the variance is non-zero. The prediction at any point is given by a normal distribution with a mean and variance. The uncertainty inherent in these predictions can be captured by sampling of the GP model hyperparameters, which can then be used in GSA. The model uncertainty pertaining to the GP model is propagated to the Sobol' index estimations using the following estimator (see [7]):

$$S_{m,n}^{X_{d_1}} = \frac{V_{m,n}^{X_{d_1}}}{V_{m,n}} = \frac{\frac{1}{m} \sum_k Z_n(X_k) Z_n(\bar{X}_k) - \frac{1}{m} \sum_k Z_n(X_k) \frac{1}{m} \sum_k Z_n(\bar{X}_k)}{\frac{1}{m} \sum_k Z_n(X_k)^2 - \left(\frac{1}{m} \sum_k Z_n(X_k)\right)^2}, \quad (24)$$

where  $Z$  is the Gaussian process and  $(X, \bar{X})$  are the random vectors.

The distribution of  $S_{m,n}^{X_{d_1}}$  can be obtained as follows:

---

**Algorithm 1:** Estimation of the distribution of  $S_{m,n}^{X_{d_1}}$ .

---

1. Build  $Z_n(x)$

**Result:** Write here the result

initialization;

**while** *While condition* **do**

    instructions;

**if** *condition* **then**

        instructions1;

        instructions2;

**else**

        instructions3;

**end**

**end**

---

A similar approach is implemented to the DNN models with the use of MC dropout (with a given dropout rate). However, in contrast to the GP models, the sampling implementation is different in the DNN models. In the DNN models, we randomly set units of the network to zero and generate predictions using the remaining units of the network. Whereas, we sample from a multivariate normal distribution in GP models to quantify the uncertainty in the Sobol' index estimates with prediction intervals.

In summary, two types of ML models are considered, namely GP and DNN models, for GSA by effectively fusing physics knowledge and experimental data to maximize the accuracy and minimize the uncertainty of the sensitivity estimates. Eight different PIML models are developed by leveraging the two PIML strategies. The effect of ML model uncertainty on the Sobol' index estimates can be quantified using the algorithm described above.

#### 4. Numerical illustration

An additive manufacturing application is used to illustrate the proposed PIML models for GSA and compare their performance. A commercial material Ultimaker Black Acrylonitrile butadiene styrene (ABS) was extruded from an Ultimaker 2 Extended+ 3D printer to manufacture fused filament fabrication (FFF) parts with unidirectionally aligned filaments and then measured with appropriate diagnostic techniques. FFF is a widely used additive manufacturing (AM) process due to its easy operation, low cost, and suitability for complex geometries. As the molten filament is deposited layer upon layer through a nozzle, it cools down, solidifies and bonds with the surrounding filaments. Rectangular specimens of length 35 mm, width 12 mm, and thickness 4.2 mm are manufactured for the ABS amorphous polymer, with constant filament height, width and length (0.7, 0.8, and 35 mm, respectively).

The output quantity of interest is porosity of the printed part, and the inputs are two process parameters, namely nozzle temperature and speed. The porosity of an FFF part is dependent on the temperature history at the interfaces between filaments. Thus, it is important to predict the temperature evolution of filaments for estimating the final mesostructure of the printed part. The analytical solution proposed by Costa et al. [42] for transient heat transfer during the printing process in FFF is used to predict the temperature evolution of filaments. A physics-based sintering model is developed, which considers realistic filament geometry, and allows the filament geometry to change during the printing process. This model is used to predict the porosity of the FFF part using the temperature evolution of filaments, material properties, part geometry, and process parameters as inputs. Thus the mapping from input to output is a multi-physics model, i.e., models of two physical phenomena (heat transfer and sintering) are combined to predict the porosity given the values of two process parameters: extrusion temperature and extrusion speed.

The statistical properties of the QoI were observed to have negligible variability along the length of the specimens; therefore the porosity measurements were taken at the midpoint cross-section (see Fig. 3) of each part with the use of microscopy images processed through the ImageJ software [43]. Filaments were extruded through a nozzle with 0.8 mm diameter. The build plate

414 temperature was constant and set to 110°C. Using Latin hypercube sampling, 39 sets of process  
 415 parameters  $\mathbf{X}$  were generated, and experiments were conducting at these 39 values. The ranges  
 416 considered for the two process variables were: printer extrusion temperature  $T$ : (210°C - 260°C),  
 and extrusion speed  $S$ : (15 mm/s - 46 mm/s).

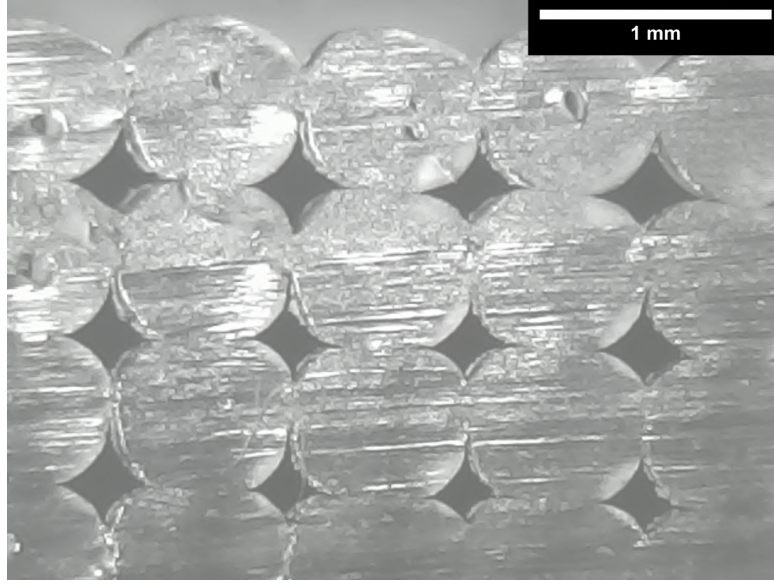


**Fig. 3.** Cross-sectional geometry of an FFF part printed with an extrusion temperature 240°C, speed 42 mm/s.

417 The basic ML models, namely Model 1 (for GP) and Model 5 (for DNN) are simply trained with the 38 sets of process inputs (temperature and speed) and output (porosity). In the training of Model 2  $\text{GP}^{\mathcal{L}_{\text{phy}}}$  and Model 6  $\text{DNN}^{\mathcal{L}_{\text{phy}}}$ , we impose two physics-based loss functions (i.e., two separate physics relationships,  $\mathcal{L}_{\text{phy},k}(\hat{\mathbf{Y}})$ , where  $k = \{1, 2\}$  and  $\hat{\mathbf{Y}}$  is the porosity prediction). The physical inconsistencies in the model predictions are evaluated using the physics-based loss functions defined as follows:

$$\begin{aligned}\mathcal{L}_{\text{phy},1}(\hat{\mathbf{Y}}) &= \frac{1}{N} \sum_{i=1}^N \text{ReLU}(-\hat{Y}_i), \\ \mathcal{L}_{\text{phy},2}(\hat{\mathbf{Y}}) &= \frac{1}{N} \sum_{i=1}^N \text{ReLU}(\hat{Y}_i - \phi_{0,i}),\end{aligned}\tag{25}$$

418 where these loss functions consider the physical violations related to the porosity across  $N$   
 419 samples. In the first loss function, a negative value of porosity is treated as a physical violation.

420 The second loss function penalizes the model when the predicted final porosity  $\hat{Y}_i$  is greater than  
 421 the initial porosity  $\phi_{0,i}$  of  $i$ th part. This is based on the physics knowledge that the total void  
 422 area decreases as the bond formation takes place. Thus, the porosity predictions are ensured to  
 423 be physically meaningful with the inclusion of these physics-based penalty terms.

424 In Model 3  $\text{GP}^{\text{upd}}$  and Model 7  $\text{DNN}^{\text{upd}}$ , the ML models are pre-trained using the multi-  
 425 physics model input-output. The pre-trained ML models are then updated using the experimen-  
 426 tal data. The training data for pre-training consists of 1310 input parameter combinations over  
 427 a range of experimental values, i.e.,  $(210^\circ\text{C} \leq T \leq 260^\circ\text{C}, 15 \text{ mm/s} \leq S \leq 46 \text{ mm/s})$ . (Note  
 428 that there are only 39 physical experiments are available; this is one of the advantages of the  
 429 pre-training/updating strategy, where the pre-training can be over a much larger set of input  
 430 combinations, thus improving the generalization performance of the updated model). The input  
 431 data are normalized prior to the training of the ML models (i.e., the output quantity porosity  
 432 is dimensionless and between 0 and 1).

Model 4 is a combination of the two strategies for GP, in which two GP models are trained;  
 (i) the first GP model trained using the physics model input-output samples consisting of 1310  
 input parameter combinations; and (ii) the second GP model is built for the discrepancy between  
 the first GP model predictions and the actual system response using the experimental data while  
 maximizing the function shown in Eq. 26 to optimize the hyperparameters of the second GP  
 model:

$$\mathcal{L}_{\overline{\text{GP}}} = \mathcal{L}_{\text{GP}} + \lambda_{\text{phy},1}^{\text{GP}} \mathcal{L}_{\text{phy},1}(\hat{\mathbf{Y}}) + \lambda_{\text{phy},2}^{\text{GP}} \mathcal{L}_{\text{phy},2}(\hat{\mathbf{Y}}). \quad (26)$$

Model 8  $\text{DNN}^{\text{upd}, \mathcal{L}_{\text{phy}}}$ , which is a combination of the two PIML strategies, uses the DNN  
 model parameters trained using the physics model input-output as the initial values. Then,  
 during the updating phase with the experimental data, these parameters are updated by mini-  
 mizing the following loss function:

$$\mathcal{L}_{\overline{\text{DNN}}} = \mathcal{L}_{\text{DNN}} + \lambda_{\text{phy},1}^{\text{DNN}} \mathcal{L}_{\text{phy},1}(\hat{\mathbf{Y}}) + \lambda_{\text{phy},2}^{\text{DNN}} \mathcal{L}_{\text{phy},2}(\hat{\mathbf{Y}}). \quad (27)$$

433 The computational costs of different models for training and estimation of Sobol' indices  
434 based on 5000 MC samples with a fixed number of experimental data ( $n = 38$ ) is given in  
435 Table. 1. The time it takes for training as well as computation of Sobol' indices using the GP  
436 models 2-4 is significantly greater than model 1. The reason for the difference between the  
437 training time of GP and  $\text{GP}^{\text{upd}}$  is the pre-training phase, where a large amount of physics input-  
438 output samples used. Whereas, the difference between the training time of GP and  $\text{GP}^{\mathcal{L}_{\text{phy}}}$   
439 due to the inclusion of physics constraints, which makes it harder for the optimization to find  
440 optimal hyperparameters. Whereas, the computation time for training of each DNN model is  
441 on average 15 sec using a desktop computer (Intel® Xeon® CPU E5-1660 v4@3.20GHz with 32  
442 GB RAM and GPU NVIDIA Quadro K620 with 2 GB) and the Sobol' index estimations based  
443 on 5000 samples take approximately 1-2 minutes for the DNN models (models 5-8). In general,  
444 GP predictions take longer because the covariance matrix needs to be stored and inverted.

**Table 1**

Computational effort of eight models for training and estimation of first-order and total-effect Sobol' indices using 5000 MC samples with  $n = 38$  number of observations.

Models	Training time	Evaluation of the distribution of $S_{m,n}^{X_{d_1}}$ [in minutes]
GP	50 sec	3
$\text{GP}^{\mathcal{L}_{\text{phy}}}$	122 sec	5
$\text{GP}^{\text{upd}}$	165 sec	7
$\text{GP}^{\text{upd}, \mathcal{L}_{\text{phy}}}$	195 sec	8
DNN	20 sec	1
$\text{DNN}^{\mathcal{L}_{\text{phy}}}$	45 sec	2
$\text{DNN}^{\text{upd}}$	30 sec	2
$\text{DNN}^{\text{upd}, \mathcal{L}_{\text{phy}}}$	55 sec	2

#### 445 4.1. GSA using GP models

446 The four GP models (Models 1 to 4) were implemented using Python. The optimization of the  
447 hyperparameters were performed using scikit-optimize package. The multipliers of the physics  
448 constraint terms of models 2 ( $\text{GP}^{\mathcal{L}_{\text{phy}}}$ ) and 4 ( $\text{GP}^{\text{upd}, \mathcal{L}_{\text{phy}}}$ ) are chosen as  $(\lambda_{\text{phy},1}^{\text{GP}}, \lambda_{\text{phy},2}^{\text{GP}}) = (50, 50)$ .  
449 The standard deviation of the observation error is assumed to be 0.001. Automatic Relevance  
450 Determination (ARD) squared exponential is used as the covariance function for all GP models.



451 The Sobol' index computations with the GP models (1-4) are based on 5000 MC samples and  
452 100 realizations of the Gaussian process.

453 The effect of the number of observations on the first-order Sobol' index estimates (for the  
454 two process inputs: extrusion temperature  $T$  and extrusion speed  $S$ ) for the four GP models is  
455 illustrated in Fig. 4. The mean values of sensitivity estimates based on the GP model predictions  
456 are denoted with solid dots at given number of observations  $n$ . The 95% prediction intervals  
457 are represented with bars above and below the solid dots for the corresponding model. The  
458 bounds in the sensitivity estimates are calculated using the mean predictions based on the 100  
459 realizations of the GP models.

460 The effect of the number of observations on the first-order Sobol' index estimates (for the  
461 two process inputs: extrusion temperature  $T$  and extrusion speed  $S$ ) for the four GP models is  
462 illustrated in Fig. 4. The total-effect sensitivity estimates of GP models for different number of  
463 experimental training data is shown in Fig. 5. The prediction intervals decrease as increasing  
464 amounts of experimental data are used to train the GP models. Further, all four models converge  
465 to similar first-order and total-effect sensitivity estimates for both printer extrusion temperature  
466 and speed. The relative contribution of extrusion speed to the variance of the porosity ( $\approx 0.65$ )  
467 is greater than that of the extrusion temperature ( $\approx 0.25$ ) and their sum is close to unity. Since  
468 the total-effects capture parameter interactions, their sum is slightly above unity, which means  
469 the parameter interactions inherent within the model do not contribute significant additional  
470 sources of uncertainty.

471 The prediction bounds of first-order sensitivity estimates of extrusion temperature obtained  
472 using 100 realizations of the GP models are shown in Table 2. The results indicate that prediction  
473 intervals obtained using models 3 and 4 ( $\text{GP}^{\text{upd}}$  and  $\text{GP}^{\text{upd}, \mathcal{L}_{\text{phy}}}$ ) converge to the bounds obtained  
474 using 38 number of observations for training the models faster than the first two models. Note  
475 that the upper 95% bound for model 2  $\text{GP}^{\mathcal{L}_{\text{phy}}}$  converge to its final value (0.33) within 10 number  
476 of observations.

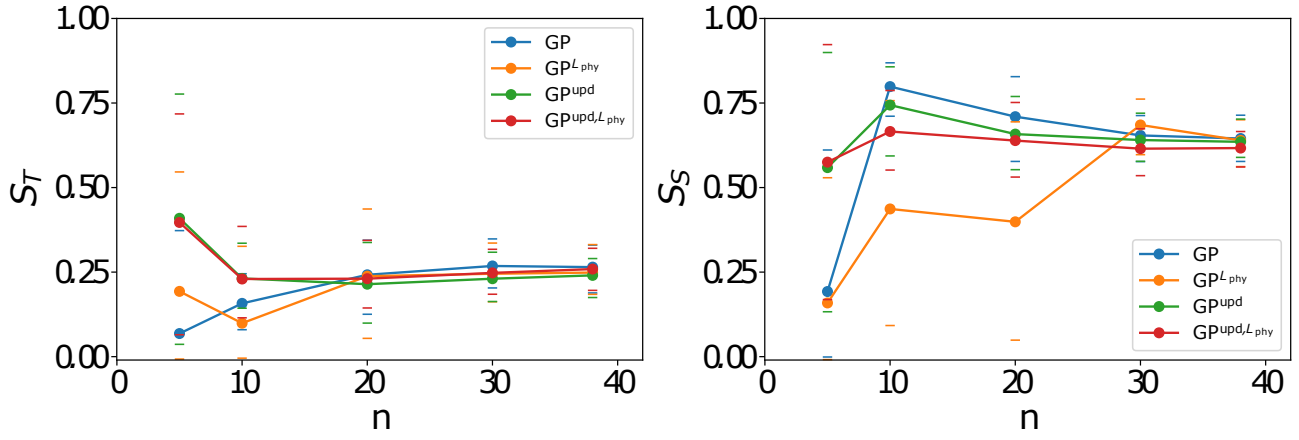


**Fig. 4.** First-order sensitivity index estimators for (a) extrusion temperature, and (b) extrusion speed, using GP models.

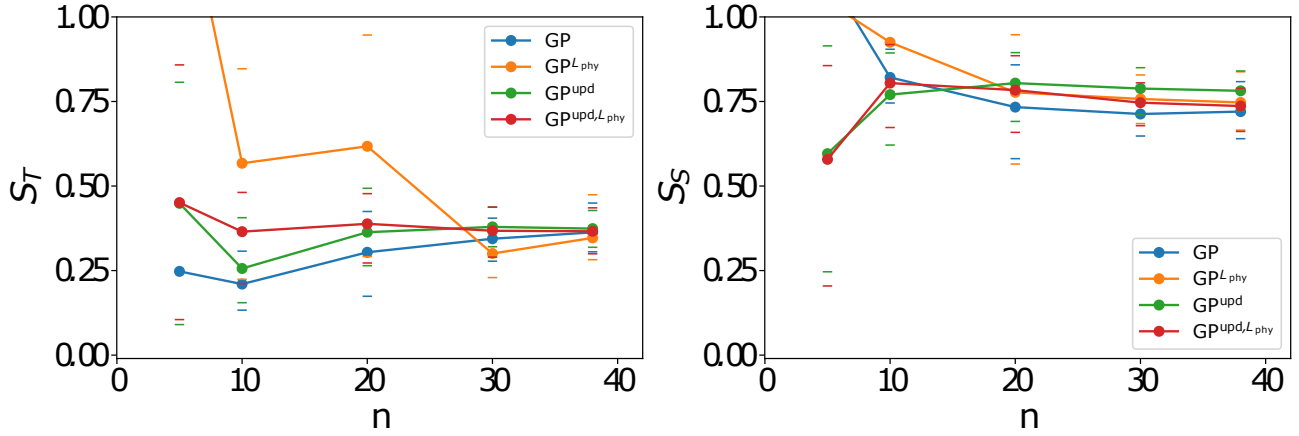


**Fig. 5.** Total-effect sensitivity index estimators for (a) extrusion temperature, and (b) extrusion speed, using GP models.

**Table 2**

First-order sensitivity estimate prediction bounds of extrusion temperature for different number of experimental training data using GP models.

Models	Lower 95% confidence limit					Upper 95% confidence limit				
	n=5	n=10	n=20	n=30	n=38	n=5	n=10	n=20	n=30	n=38
GP	-0.01	0.08	0.13	0.20	0.19	0.37	0.25	0.34	0.35	0.33
$GP^{\mathcal{L}_{phy}}$	-0.01	-0.01	0.05	0.16	0.18	0.55	0.33	0.43	0.34	0.33
$GP^{upd}$	0.03	0.14	0.10	0.16	0.17	0.77	0.33	0.34	0.31	0.29
$GP^{upd,\mathcal{L}_{phy}}$	0.06	0.11	0.14	0.18	0.20	0.71	0.38	0.34	0.31	0.32

#### 4.2. GSA using DNN models with MC dropout

The four DNN models (Models 5 to 8) were implemented using the Keras package [44] with Tensorflow in the backend. The hyperparameters of each model are tuned with grid search and

the multipliers of the physics constraint terms in Model 6 ( $\text{DNN}^{\mathcal{L}_{\text{phy}}}$ ) and Model 8 ( $\text{DNN}^{\text{upd}, \mathcal{L}_{\text{phy}}}$ ) are chosen as  $(\lambda_{\text{phy},1}^{\text{DNN}}, \lambda_{\text{phy},2}^{\text{DNN}}) = (0.01, 0.01)$ . Fully-connected DNN models with 2 hidden layers and 5 neurons in each hidden layer are constructed. The Rectified Linear Unit (ReLU) activation function and Adam optimizer are used to perform stochastic gradient descent for 300 epochs in learning the model parameters. The Sobol' index computations with the DNN models (5-8) are based on 5000 MC samples and 100 stochastic forward passes through the networks.

The DNN models without MC dropout maps deterministic inputs to a deterministic output. On the other hand, DNN models with MC dropout maps deterministic inputs to a stochastic output. Therefore, instead of unique Sobol' index values, distribution of sensitivity estimates are obtained. DNN models with MC dropout results in bounds for the sensitivity estimates as opposed to DNN models without MC dropout.

The effect of dropout rate  $p_d$  for a fixed number of observations ( $n=38$ ) in the first-order Sobol' index estimates of DNN models using MC dropout is shown in Fig. 6. The total-effect Sobol' index estimates of DNN models using MC dropout with different dropout rates for  $n = 38$  is given in Fig. 7. The values of first-order sensitivity index obtained using DNN models with MC dropout for extrusion temperature and extrusion speed decrease with increasing dropout rates except the range (0.0-0.05). Whereas, the values of total-effect sensitivity index obtained using DNN models with MC dropout for extrusion temperature and extrusion speed monotonically increase with increasing dropout rates except the range (0.0-0.05). These results show that the dropout rate is also needed to be optimized along with the model parameters to be able to achieve accurate sensitivity estimates.

The dropout rate is chosen based on the model prediction accuracy. The RMSE values of DNN models with MC dropout for different dropout rates are shown in Fig. 8. The lowest RMSE values for all four models are obtained between 0.005-0.05. Based on these results, the dropout rate for all the MC dropout simulations is chosen to be 0.05.

The calculated first-order sensitivity estimates of temperature and speed,  $S_T$  and  $S_S$  respectively, for different number of observations  $n = (5, 10, 20, 30, 38)$  are shown in Fig. 9. The distribution of sensitivity estimates are obtained using MC dropout predictions based on 100

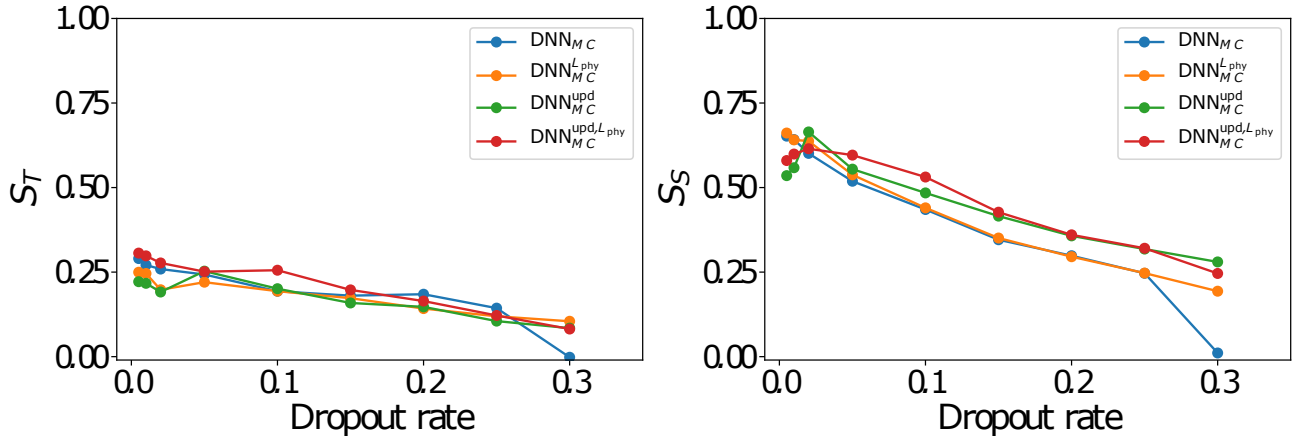


**Fig. 6.** First-order sensitivity index estimators for (a) extrusion temperature, and (b) extrusion speed, using DNN models with MC dropout.

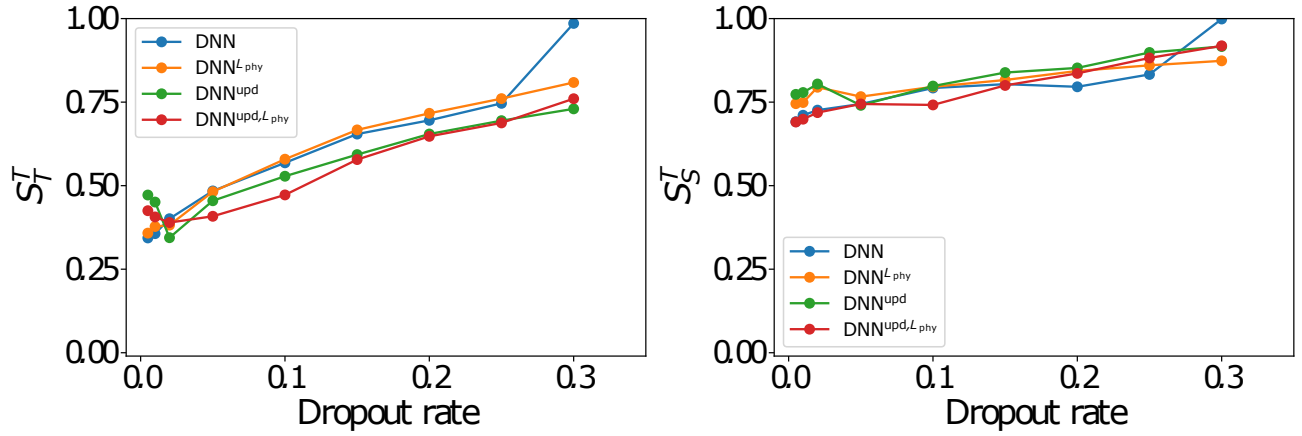


**Fig. 7.** Total-effect sensitivity index estimators for (a) extrusion temperature, and (b) extrusion speed, using DNN models with MC dropout.

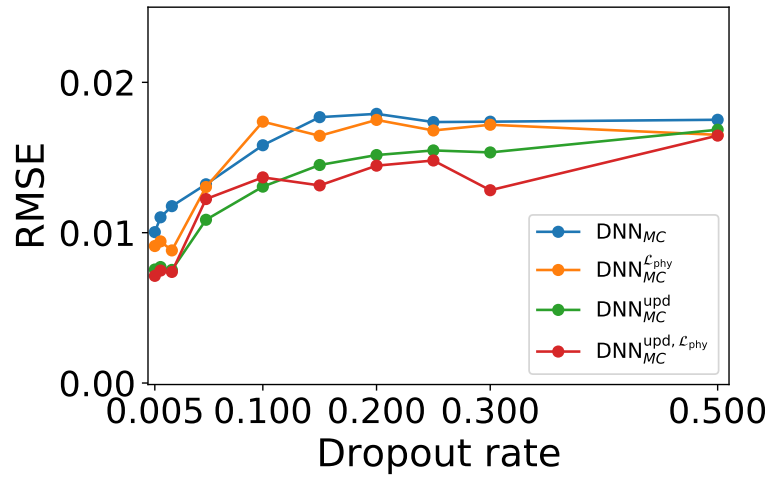


**Fig. 8.** RMSE values of DNN models with varying dropout rates.

stochastic forward passes through the networks for different number of observations. The mean values of sensitivity estimates are represented with solid dots and the 95% bounds are denoted with bars above and below the solid dots for the corresponding model. Similarly, the calculated total-effect sensitivity estimates  $S_T$  and  $S_S$  for different number of  $n$  are illustrated in Fig. 10. The difference between the total-effect and first-order effects of process inputs is negligible, which indicates that the parameter interactions are not significant.

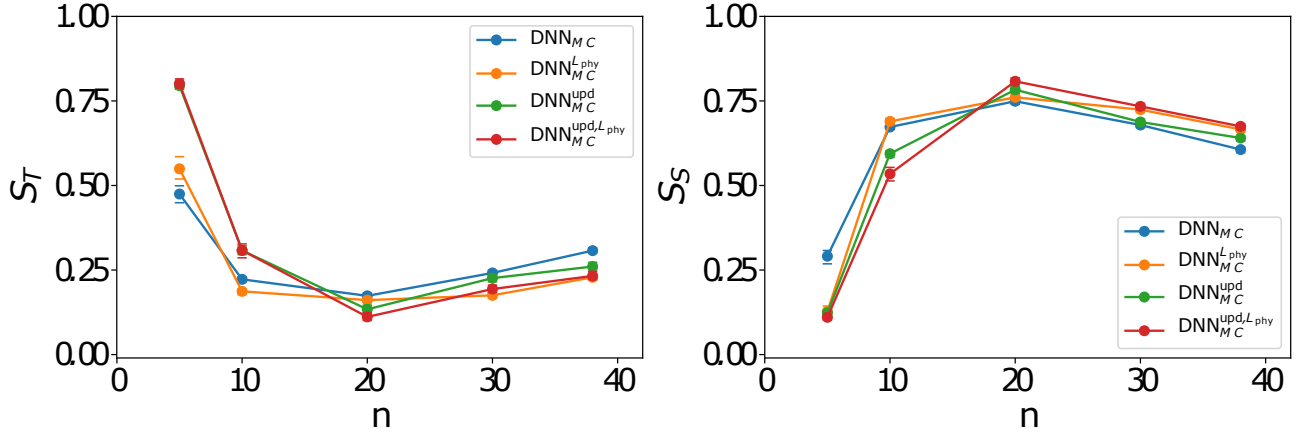


**Fig. 9.** First-order sensitivity index estimators for (a) extrusion temperature, and (b) extrusion speed, using DNN models with MC dropout.

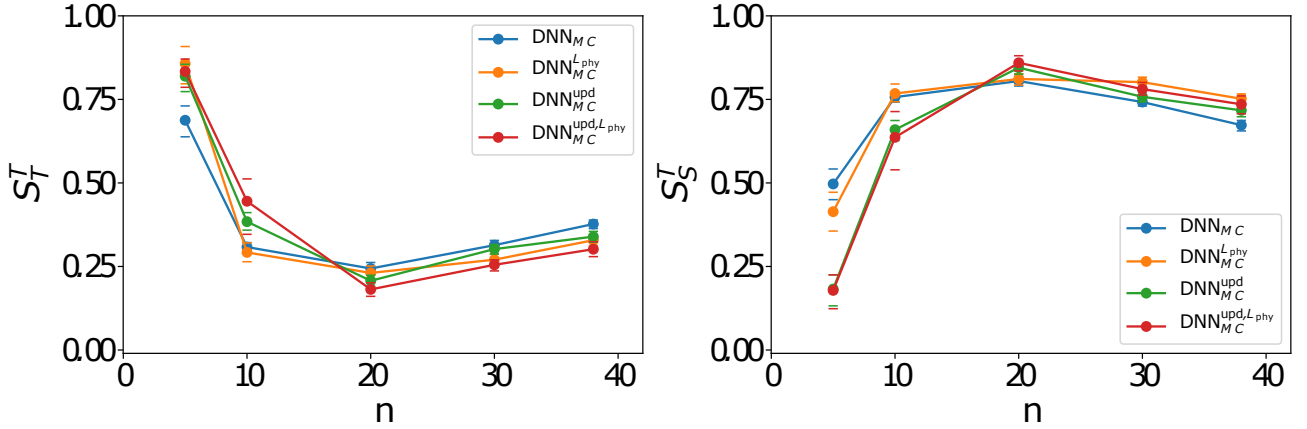


**Fig. 10.** Total-effect sensitivity index estimators for (a) extrusion temperature, and (b) extrusion speed, using DNN models with MC dropout.

All DNN models converge to similar first-order and total-effect sensitivity estimates for both input parameter and these values are consistent with the results obtained using GP models. The relative contribution of extrusion speed to the variance of the porosity ( $\approx 0.65$ ) is greater

517 than that of the extrusion temperature ( $\approx 0.25$ ). The prediction intervals decrease as increasing  
518 amounts of experimental data are used to train the DNN models.

519 The prediction intervals obtained using the DNN models are much narrower than the ones  
520 obtained using GP models since the DNN models has more degrees of freedom that can be  
521 optimized. For instance, the number of epochs, which is the number of complete passes through  
522 a batch of training dataset, is optimized for DNN models; thus, the prediction accuracy of  
523 each model is maximized. The maximization of the prediction accuracy of the DNN models  
524 through the use of optimal number of epochs allowed the sensitivity estimates to have narrow  
525 bounds. The main difference between the results obtained using GP and DNN models is that  
526 the sensitivity estimates evaluated based on the DNN model predictions do not show a strong  
527 convergence, which may be because of the noisy data or the quantity of the data. Further, the  
528 DNN models has many more parameters than the GP models. More specifically, GP models have  
529 at most 5 parameters to optimize, whereas the DNN models have 23 model parameters and other  
530 parameters such as the number of epochs, dropout rate, etc. Since the DNN models have many  
531 degrees of freedom, it requires a greater number of observations for the sensitivity estimates  
532 to converge for the DNN models compared to the GP models. The number of parameters  
533 to be learned reduces with the use of dropout, which helps with regularization and prevents  
534 ill-conditioning.

## 535 5. Conclusion

536 This paper developed methodologies for information fusion and machine learning for sen-  
537 sitivity analysis using physics knowledge and experimental data, while accounting for model  
538 uncertainty. Variance-based sensitivity analysis is used to quantify the relative contribution of  
539 each uncertainty source to the variability of the output quantity. Two types of ML models were  
540 considered, namely, GP and DNN models. Several PIML models were developed by leverag-  
541 ing two strategies for incorporating physics knowledge into ML models: (1) incorporating loss  
542 functions in the ML models to enforce physics constraints, and (2) pre-training an ML model  
543 with simulation data and then updating it with experimental data. The effect of ML model

uncertainty on the sensitivity index estimate is analyzed, and the accuracy and computational of the various PIML models are compared.

The results show that the application of PIML strategies to both GP and DNN allows accurate Sobol' index computations even with smaller amounts of experimental data while producing physically meaningful results. Thus, the proposed approach helps to fill the physics knowledge gap in the ML models while estimating the Sobol' indices, by correcting for the approximation in the physics-based models. The numerical example shows that training the GP models for estimating the Sobol' indices require more computational effort than the DNN models and the uncertainty regarding the sensitivity estimates obtained using the DNN models is smaller than the results obtained using the GP models.

In future work, the proposed framework needs to be tested for problems with a larger number of dimensions both in the input and output, with multiple combinations to further analyze the convergence of Sobol' index estimates for different PIML strategies. Future work can also explore the weighting of the two sources of data since the data produced by physics-based models and experiments have different levels of credibility.

## References

- [1] A. Saltelli, M. Ratto, T. Andres, F. Campolongo, J. Cariboni, D. Gatelli, M. Saisana, S. Tarantola, Global sensitivity analysis: the primer, John Wiley & Sons, 2008.
- [2] A. Saltelli, S. Tarantola, K.-S. Chan, A quantitative model-independent method for global sensitivity analysis of model output, *Technometrics* 41 (1) (1999) 39–56.
- [3] T. A. Mara, S. Tarantola, Variance-based sensitivity indices for models with dependent inputs, *Reliability Engineering & System Safety* 107 (2012) 115–121.
- [4] E. Borgonovo, E. Plischke, Sensitivity analysis: a review of recent advances, *European Journal of Operational Research* 248 (3) (2016) 869–887.
- [5] S. Sankararaman, S. Mahadevan, Separating the contributions of variability and parameter

uncertainty in probability distributions, *Reliability Engineering & System Safety* 112 (2013) 187–199.

[6] C. Li, S. Mahadevan, Relative contributions of aleatory and epistemic uncertainty sources in time series prediction, *International Journal of Fatigue* 82 (2016) 474–486.

[7] L. Le Gratiet, C. Cannamela, B. Iooss, A bayesian approach for global sensitivity analysis of (multifidelity) computer codes, *SIAM/ASA Journal on Uncertainty Quantification* 2 (1) (2014) 336–363.

[8] J. E. Oakley, A. O’Hagan, Probabilistic sensitivity analysis of complex models: a bayesian approach, *Journal of the Royal Statistical Society: Series B (Statistical Methodology)* 66 (3) (2004) 751–769.

[9] A. Marrel, B. Iooss, B. Laurent, O. Roustant, Calculations of sobol indices for the gaussian process metamodel, *Reliability Engineering & System Safety* 94 (3) (2009) 742–751.

[10] Z. Hu, S. Mahadevan, Probability models for data-driven global sensitivity analysis, *Reliability Engineering & System Safety* 187 (2019) 40–57.

[11] A. Marrel, B. Iooss, F. Van Dorpe, E. Volkova, An efficient methodology for modeling complex computer codes with gaussian processes, *Computational Statistics & Data Analysis* 52 (10) (2008) 4731–4744.

[12] A. O’Hagan, Bayesian analysis of computer code outputs: A tutorial, *Reliability Engineering & System Safety* 91 (10-11) (2006) 1290–1300.

[13] I. M. Sobol, Global sensitivity indices for nonlinear mathematical models and their monte carlo estimates, *Mathematics and computers in simulation* 55 (1-3) (2001) 271–280.

[14] B. Sudret, Global sensitivity analysis using polynomial chaos expansions, *Reliability engineering & system safety* 93 (7) (2008) 964–979.



- [15] W. Chen, R. Jin, A. Sudjianto, Analytical variance-based global sensitivity analysis in simulation-based design under uncertainty (2005).
- [16] S. Tarantola, D. Gatelli, T. A. Mara, Random balance designs for the estimation of first order global sensitivity indices, *Reliability Engineering & System Safety* 91 (6) (2006) 717–727.
- [17] F. Satterthwaite, Random balance experimentation, *Technometrics* 1 (2) (1959) 111–137.
- [18] E. C. DeCarlo, S. Mahadevan, B. P. Smarslok, Efficient global sensitivity analysis with correlated variables, *Structural and Multidisciplinary Optimization* 58 (6) (2018) 2325–2340.
- [19] V. Ginot, S. Gaba, R. Beaudouin, F. Aries, H. Monod, Combined use of local and anova-based global sensitivity analyses for the investigation of a stochastic dynamic model: application to the case study of an individual-based model of a fish population, *Ecological modelling* 193 (3-4) (2006) 479–491.
- [20] G. Archer, A. Saltelli, I. Sobol, Sensitivity measures, anova-like techniques and the use of bootstrap, *Journal of Statistical Computation and Simulation* 58 (2) (1997) 99–120.
- [21] C. Li, S. Mahadevan, An efficient modularized sample-based method to estimate the first-order sobol’ index, *Reliability Engineering & System Safety* 153 (2016) 110–121.
- [22] A. Karpatne, W. Watkins, J. Read, V. Kumar, Physics-guided neural networks (pgnn): An application in lake temperature modeling, *arXiv preprint arXiv:1710.11431* (2017).
- [23] X. Jia, J. Willard, A. Karpatne, J. S. Read, J. A. Zwart, M. Steinbach, V. Kumar, Physics-guided machine learning for scientific discovery: An application in simulating lake temperature profiles, *arXiv preprint arXiv:2001.11086* (2020).
- [24] J. Willard, X. Jia, S. Xu, M. Steinbach, V. Kumar, Integrating physics-based modeling with machine learning: A survey, *arXiv preprint arXiv:2003.04919* (2020).

- [25] L. L. Gratiet, S. Marelli, B. Sudret, Metamodel-based sensitivity analysis: polynomial chaos expansions and gaussian processes, arXiv preprint arXiv:1606.04273 (2016).
- [26] A. Marrel, B. Iooss, S. Da Veiga, M. Ribatet, Global sensitivity analysis of stochastic computer models with joint metamodels, *Statistics and Computing* 22 (3) (2012) 833–847.
- [27] D. Xiu, G. E. Karniadakis, The wiener–askey polynomial chaos for stochastic differential equations, *SIAM journal on scientific computing* 24 (2) (2002) 619–644.
- [28] A. Janon, M. Nodet, C. Prieur, Uncertainties assessment in global sensitivity indices estimation from metamodels, *International Journal for Uncertainty Quantification* 4 (1) (2014).
- [29] Z. Hu, X. Du, Mixed efficient global optimization for time-dependent reliability analysis, *Journal of Mechanical Design* 137 (5) (2015).
- [30] N. Muralidhar, M. R. Islam, M. Marwah, A. Karpatne, N. Ramakrishnan, Incorporating prior domain knowledge into deep neural networks, in: 2018 IEEE International Conference on Big Data (Big Data), IEEE, 2018, pp. 36–45.
- [31] M. C. Kennedy, A. O’Hagan, Bayesian calibration of computer models, *Journal of the Royal Statistical Society: Series B (Statistical Methodology)* 63 (3) (2001) 425–464.
- [32] Y. Ling, J. Mullins, S. Mahadevan, Selection of model discrepancy priors in bayesian calibration, *Journal of Computational Physics* 276 (2014) 665–680.
- [33] J. S. Denker, Y. LeCun, Transforming neural-net output levels to probability distributions, in: *Advances in neural information processing systems*, 1991, pp. 853–859.
- [34] D. J. MacKay, A practical bayesian framework for backpropagation networks, *Neural computation* 4 (3) (1992) 448–472.
- [35] R. M. Neal, *Bayesian learning for neural networks*, Vol. 118, Springer Science & Business Media, 2012.

- 639 [36] C. Blundell, J. Cornebise, K. Kavukcuoglu, D. Wierstra, Weight uncertainty in neural  
640 networks, arXiv preprint arXiv:1505.05424 (2015).
- 641 [37] A. Graves, Practical variational inference for neural networks, in: Advances in neural in-  
642 formation processing systems, 2011, pp. 2348–2356.
- 643 [38] J. M. Hernández-Lobato, Y. Li, M. Rowland, D. Hernández-Lobato, T. Bui, R. Turner,  
644 Black-box  $\alpha$ -divergence minimization (2016).
- 645 [39] Y. Gal, Z. Ghahramani, Bayesian convolutional neural networks with bernoulli approximate  
646 variational inference, arXiv preprint arXiv:1506.02158 (2015).
- 647 [40] Y. Gal, Z. Ghahramani, Dropout as a bayesian approximation: Representing model un-  
648 certainty in deep learning, in: international conference on machine learning, 2016, pp.  
649 1050–1059.
- 650 [41] X. Zhang, S. Mahadevan, Bayesian neural networks for flight trajectory prediction and  
651 safety assessment, Decision Support Systems (2020) 113246.
- 652 [42] S. Costa, F. Duarte, J. Covas, Estimation of filament temperature and adhesion develop-  
653 ment in fused deposition techniques, Journal of Materials Processing Technology 245 (2017)  
654 167–179.
- 655 [43] C. A. Schneider, W. S. Rasband, K. W. Eliceiri, Nih image to imagej: 25 years of image  
656 analysis, Nature methods 9 (7) (2012) 671.
- 657 [44] F. Chollet, et al., keras. github repository, <https://github.com/fchollet/keras>. Accessed  
658 on 25 (2015) 2017.